Angewandte Chemie
Eine Zeitschrift der Gesellschaft Deutscher Chemiker

Supporting Information

Stabilizing Cobalt-free Li-rich Layered Oxide Cathodes through Oxygen Lattice Regulation by Two-phase Ru Doping

Y. Fan, E. Olsson, G. Liang, Z. Wang, A. M. D'Angelo, B. Johannessen, L. Thomsen, B. Cowie, J. Li, F. Zhang, Y. Zhao, W. K. Pang, Q. Cai*, Z. Guo**

SUPPORTING INFORMATION

Experimental Procedures

Material Synthesis

$Li_{1.2}Ni_{0.2}Mn_{0.6}O_2$ and Ru-doped $Li_{1.2}Ni_{0.2}Mn_{0.6}O_2$ were synthesized via a solid-state reaction. Specifically, stoichiometric amounts of NiO (Sigma-Aldrich 99.9%), $MnCO_3$ (Sigma-Aldrich 99.9%), and RuO_2 (Sigma-Aldrich 99.9%) were homogenized using a mortar and pestle for 20 min and then mixed with a 5% excess of Li_2CO_3 (Sigma-Aldrich) by ball milling at 300 revolutions per minute for 10 h. The resultant mixture was pelletized and calcinated at 950 °C for 15 h in air. The heating rate was 5 °C per minute. $Li_{1.2}Ni_{0.2}Mn_{0.6}O_2$, $Li_{1.2}Ni_{0.2}Mn_{0.59}Ru_{0.01}O_2$, $Li_{1.2}Ni_{0.2}Mn_{0.57}Ru_{0.03}O_2$, and $Li_{1.2}Ni_{0.2}Mn_{0.55}Ru_{0.05}O_2$ are hereinafter referred to as LNMO, LNMO-0.01Ru, LNMO-0.03Ru, and LNMO-0.05Ru, respectively. Inductively coupled plasma-atomic emission spectroscopy (ICP-AES) analysis data for the atomic compositions of the as-synthesized materials are shown in Table S4. Li:Mn:Ni ratios in the samples are consistent with the expected stoichiometry within experimental errors.

Electrochemical Testing

Electrochemical tests versus lithium metal were done in CR2032-type coin cells. For the cathode preparation, a homogeneous slurry was obtained by mixing the active material, polyvinylidene difluoride, and carbon black (super P) in a weight ratio of 8:1:1 in the solvent of N-methyl-2-pyrrolidone. The slurry was cast onto an aluminium foil and then dried at 120 °C for 12 h in a vacuum oven. The loading mass of the active materials is 1.2 ± 0.2 mg cm^{-2}. The dried electrodes were pressed and cut into circles with a diameter of 10 mm. The coin cells were assembled in an argon-filled glove box using lithium foil and Celgard 2400 polypropylene film as the counter electrode and separator, respectively. The electrolyte composition is 1 M $LiPF_6$ dissolved in ethylene carbonate and dimethyl carbonate (1:1 vol%). Galvanostatic charge/discharge testing was performed on a LAND CT-2001A instrument at ambient temperature. Galvanostatic intermittent titration technique (GITT) was also carried out, where the cells were charged/discharged for one cycle at 0.1 C to activate the materials and then charged at 0.1 C for 10 min, followed by a relaxation of 60 min open circuit. Cyclic voltammetry (CV) was measured using a Biologic VMP3 electrochemical workstation. The voltage window of scanning was between 2.0 V and 4.8 V. EIS was collected with a disturbance amplitude of 5 mV between 100 kHz and 10 mHz.

Material Characterization

Lab-based X-ray powder diffraction (XRPD) data were collected on a PANalytical Empyrean instrument with Cu Kα radiation. Neutron powder diffraction (NPD) was performed on the high-resolution neutron powder diffractometer Echidna,[1] at the Open Pool Australian Light water (OPAL) research at the Australian Nuclear Science and Technology Organisation (ANSTO). The NPD data were recorded in the 2θ range of 4-164° at a step size of 0.05° with a wavelength of 1.62348(5) Å, using the $La^{11}B_6$ National Institute of Standards and Technology standard reference material 660b. Joint Rietveld refinement against the XRPD and NPD data was performed using GSAS-II software.[2] The refined parameters include background coefficients, zero shift, peak-shape parameters, lattice parameters, scale factor, site occupancy factors of Li and Ni, atomic positional parameters, and isotropic atomic displacement parameters.
Neutron total scattering data were acquired at room temperature at the nanoscale-ordered materials diffractometer (NOMAD) beamline at the Spallation Neutron Source (SNS), Oak Ridge National Laboratory (ORNL). About 0.2g powder samples of LNMO and LNMO-0.03Ru were loaded into 3 mm quartz capillaries and sealed using clay in the air. The obtained diffraction data were normalized against a vanadium rod, and the carbon background was subtracted. The total scattering structure factor S(Q) data were then transformed to PDF G(r) data through specific IDL codes developed for the NOMAD instrument.[3] The Q range from 0.15 $Å^{-1}$ to 30 $Å^{-1}$ was used for Fourier transfer. The instrumental parameter Q_{damp} and Q_{broad} were set to be 0.01810 and 0.02542 $Å^{-1}$, respectively. The PDF fitting was performed using PDFGUI [4].
X-ray photoelectron spectroscopy (XPS) data were collected using a Thermo Scientific Nexsa X-ray photoelectron spectrometer system. C 1*s* peak (284.8 eV) was used to calibrate the XPS binding energy. For XPS characterization of the active materials, XPS data were collected after etching the samples for 300s using an Ar ion gun with an energy of 4000 eV. Scanning electron microscopy (SEM, JEOL JSM 7500) and aberration-corrected transmission electron microscopy (TEM, JEOL ARM-200F) were adopted to investigate the morphology of the active materials. Energy dispersive spectroscopy (EDS) and scanning TEM high-angle annular dark-field (STEM HAADF) were performed on the JEOL ARM-200F at 200 kV.

Post-mortem and *in operando* structural evolution studies using synchrotron techniques

SUPPORTING INFORMATION

Post-mortem characterizations of the active materials at different states of charge/discharge were carried out by extracting the positive electrode from a cycled coin cell in an argon-filled glove box, which were transferred and stored under a vacuum before use. Near-edge X-ray fine structure (NEXAFS) characterizations of the electrodes were performed at the soft X-ray beamline,[5] Australian Synchrotron, Melbourne, Australia. The NEXAFS data were processed with Igor Pro 8, with the QANT[6] add-in developed at the Australian Synchrotron. The X-ray absorption (XAS) studies were carried out at the XAS beamline of the Australian Synchrotron. The XAS data were processed using Athena.[6]

In operando XRPD measurements were performed at the Powder Diffraction beamline at the Australian synchrotron. The preparation of the coin cells for *in operando* XRPD tests can be found in the previous work of our group.[7] The synchrotron XRPD data were collected using an MYTHEN microstrip detector[8] with a continuous acquisition time of 60 s. The wavelength is 0.688762(1) Å determined by the $La^{11}B_6$ National Institute of Standards and Technology standard reference material 660b. The cells at the first cycle were charged/discharged at the current density of 0.1 C, while 0.2 C was adopted after 50 cycles. The voltage range is between 2.0 and 4.8 V.

Computational Details

All density functional theory (DFT) simulations were conducted in GPAW,[9] which is a real-space project augmented wave (PAW) code,[10] within the atomic simulation environment (ASE).[11] The exchange-correlation energy was calculated with the Perdew-Burke-Ernzerhof (PBE) generalized gradient approximation (GGA) functional for all systems.[12] To sample the Brillouin zone, a 3×3×2 Monkhorst-Pack grid for h-LNMO and a 4×2×2 grid for m-LNMO were employed.[13] The plane wave cut-off energy was set at 800 eV, both chosen after convergence tests of the total energy to 1 meV/formula unit. All simulations were performed under spin-polarised conditions. For all structural optimizations, the forces converged to 0.05 eV/$Å^{-1}$, with an electronic convergence criterion of 10^{-5} eV. For all simulations, the DFT+U formalism was used to account for the inherent self-interaction error in DFT due to the transition metal *d*-states.[14] Based on previous work, we used U_{eff} = 5.96 eV for Ni, U_{eff} = 5.10 eV for Mn, and U_{eff} = 1.50 eV for Ru.[15] This setup also shows the ground state structure of LNMO to be antiferromagnetic, in agreement with previous work.

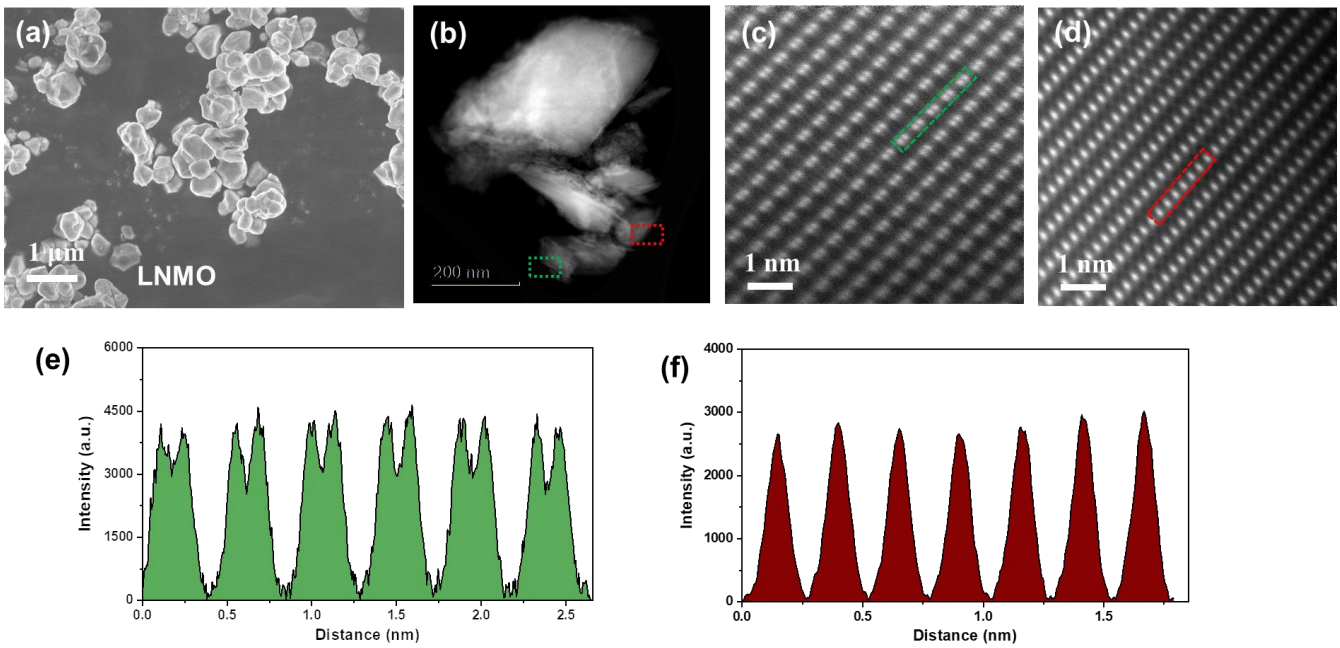

Figure S1. (a) SEM and (b) TEM images of the undoped LNMO; (c), (d) typical HAADF-STEM images corresponding to the two regions in (b) highlighted with a green box and a red box, respectively); (g) line profile analysis within the green box in (c); (f) line profile analysis within the red box in (d).

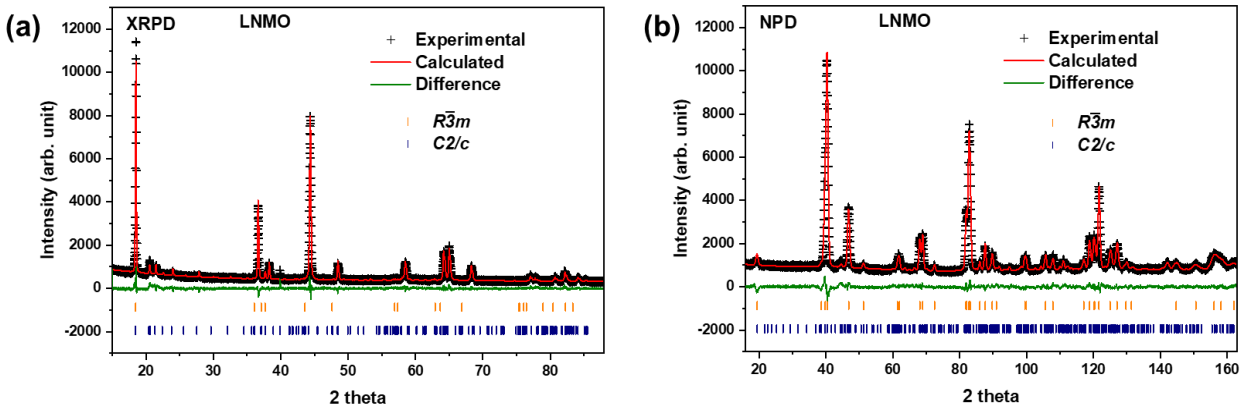

Figure S2. Joint Rietveld refinement profiles using (a) XRPD data and (b) NPD data of the undoped LNMO (R_{wp} = 5.79%, combined GOF = 1.56, the *R-3m* phase = 40(2) wt%, the *C2/c* phase = 60(2) wt%)

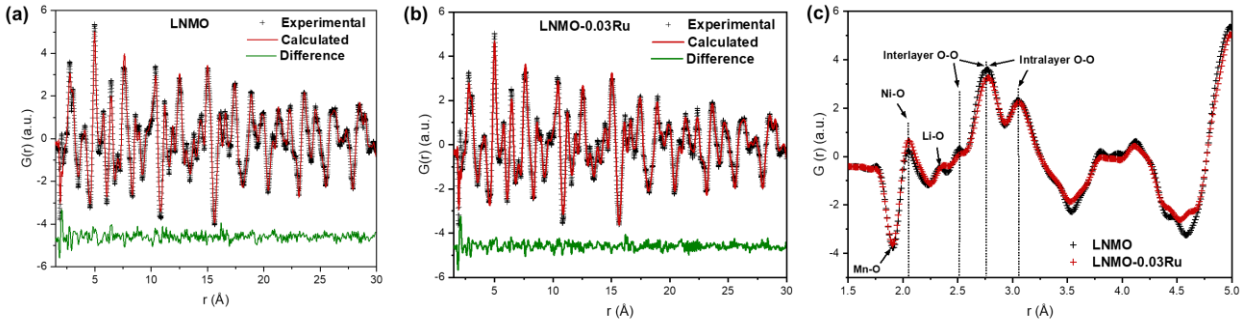

Figure S3. Refinement profiles of the (a) undoped LNMO (R_{wp} = 19.2%) and (b) LNMO-0.03Ru (R_{wp} = 19.3%) local structure using long-range Neutron PDF data. (c) Neutron PDF data of LNMO and LNMO-0.03Ru in a short range.

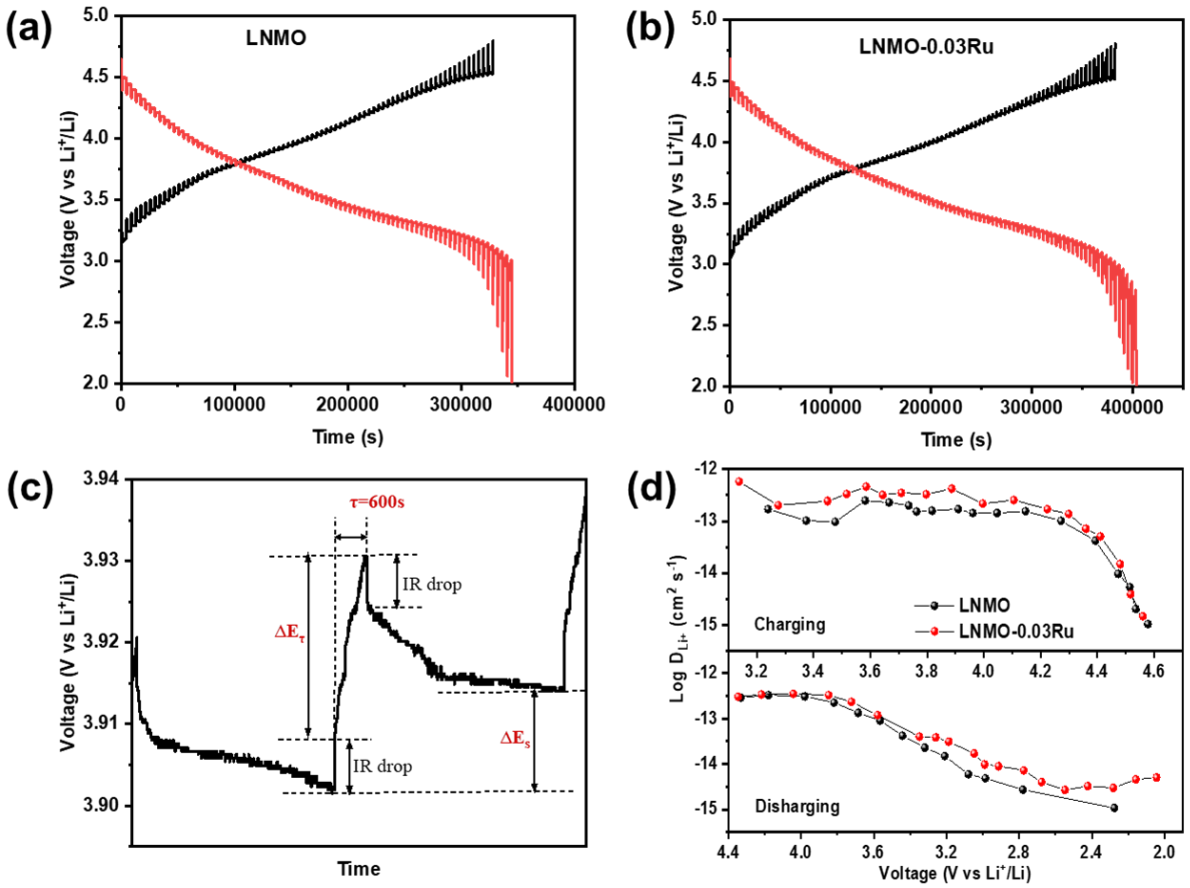

Figure S4. GITT curves of the (a) undoped LNMO and (b) LNMO-0.03Ru; (c) selected titration curves of LNMO where the IR drop, ΔE_τ, ΔE_s, and τ are defined; (d) Li-ions diffusion coefficient of undoped LNMO and LNMO-0.03Ru calculated from GITT data.

The diffusion coefficient of Li ions (D_{Li^+}) was calculated using the following equation.

$$D_{Li^+} = \frac{4}{\pi}\left(\frac{m_B V_M}{M_B A}\right)^2 \left(\frac{\Delta E_s}{\Delta E_\tau}\right)^2,$$

Where m_B and M_B correspond to the weight and molecular weight of the active material, respectively. V_M and A are the molar volume of the active material and the area of the electrode, respectively. ΔE_τ, ΔE_s, and τ are shown in Figure S5c.

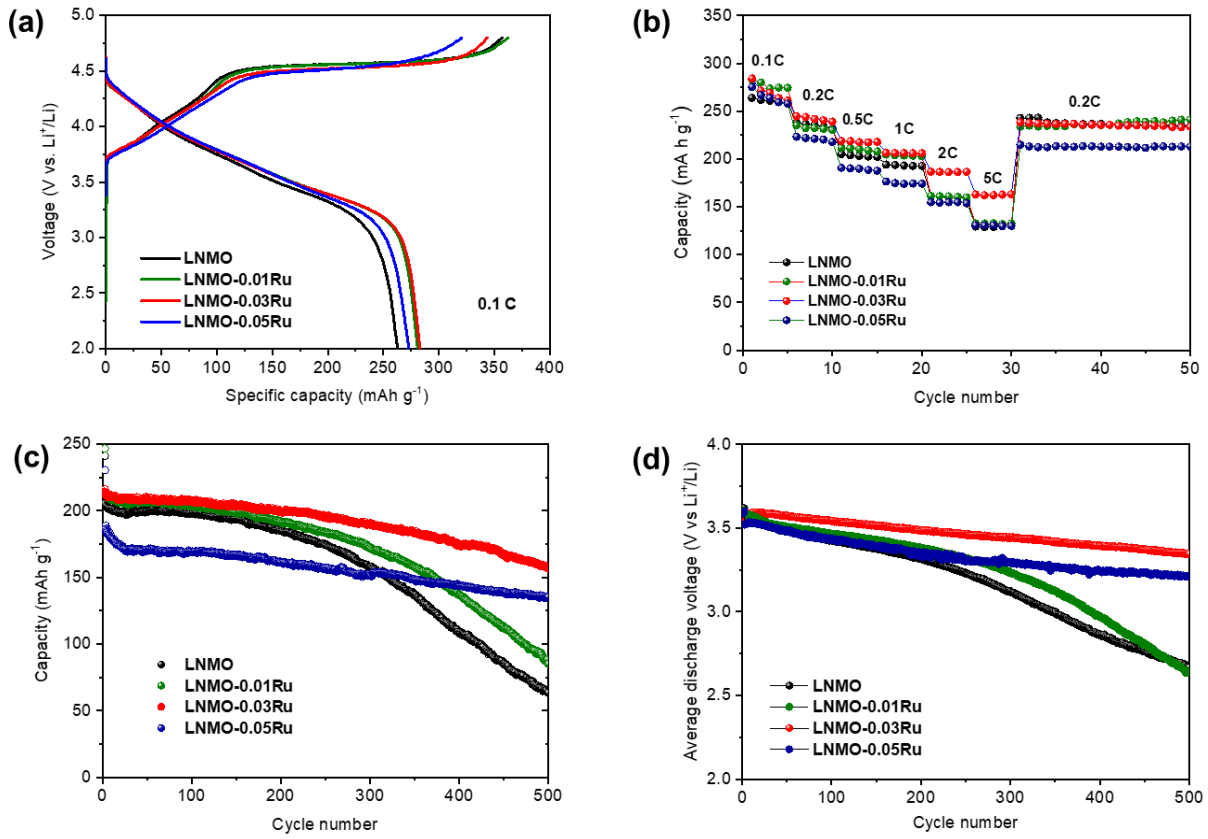

Figure S5. (a) The first charge/discharge curves at 0.1C of different LNMO samples; (b) the rate capability of the different LNMO samples; (c) cycling performance and (d) corresponding average discharge voltage of different LNMO samples at 1C.

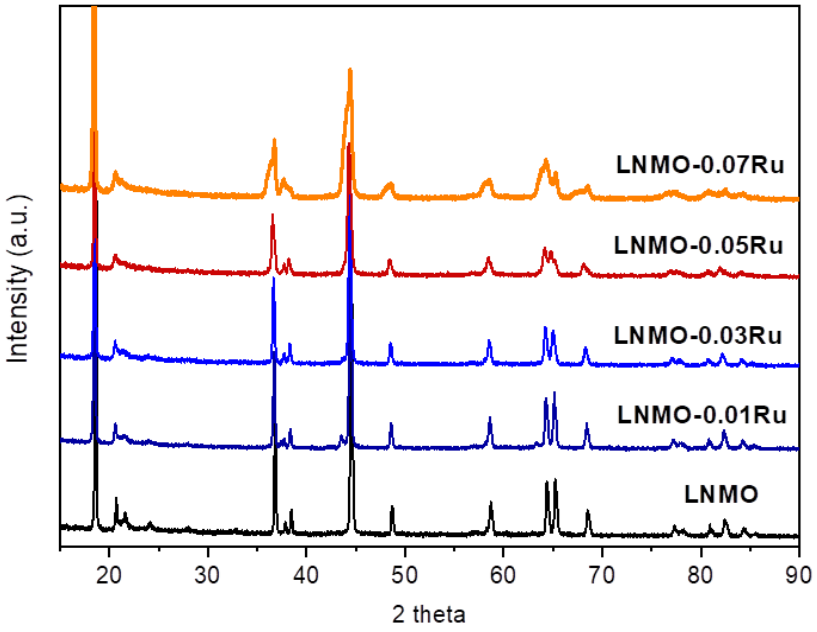

Figure S6. XRD patterns of the undoped LNMO and LNMO with different doping content.

To investigate the effects of the different Ru doping content on the crystal structure of LNMO, the XRD patterns of all the materials are shown in Figure S6. For the LNMO with 1% and 3% Ru doping, all peaks are consistent with the undoped LNMO, and a high degree of crystallization remains, indicating that Ru has been successfully doped into the layered structure of LNMO. On further increasing the doping content of Ru to 5% or 7%, the crystallization becomes poor, suggesting the formation of impurities. This might be responsible for the lower capacity of 5% Ru doping than that of LNMO-0.03Ru.

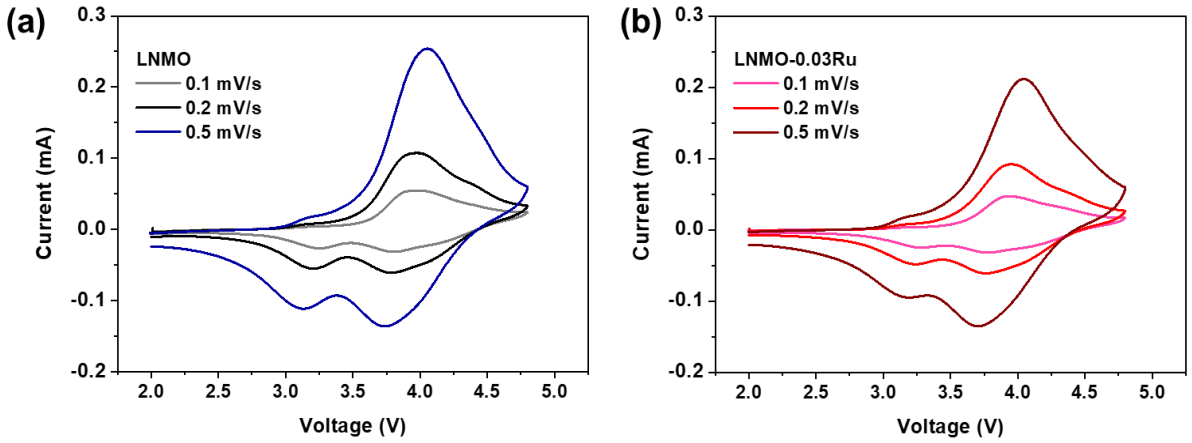

Figure S7. CV curves of the (a) undoped LNMO and (b) LNMO-0.03Ru at different scan rates.

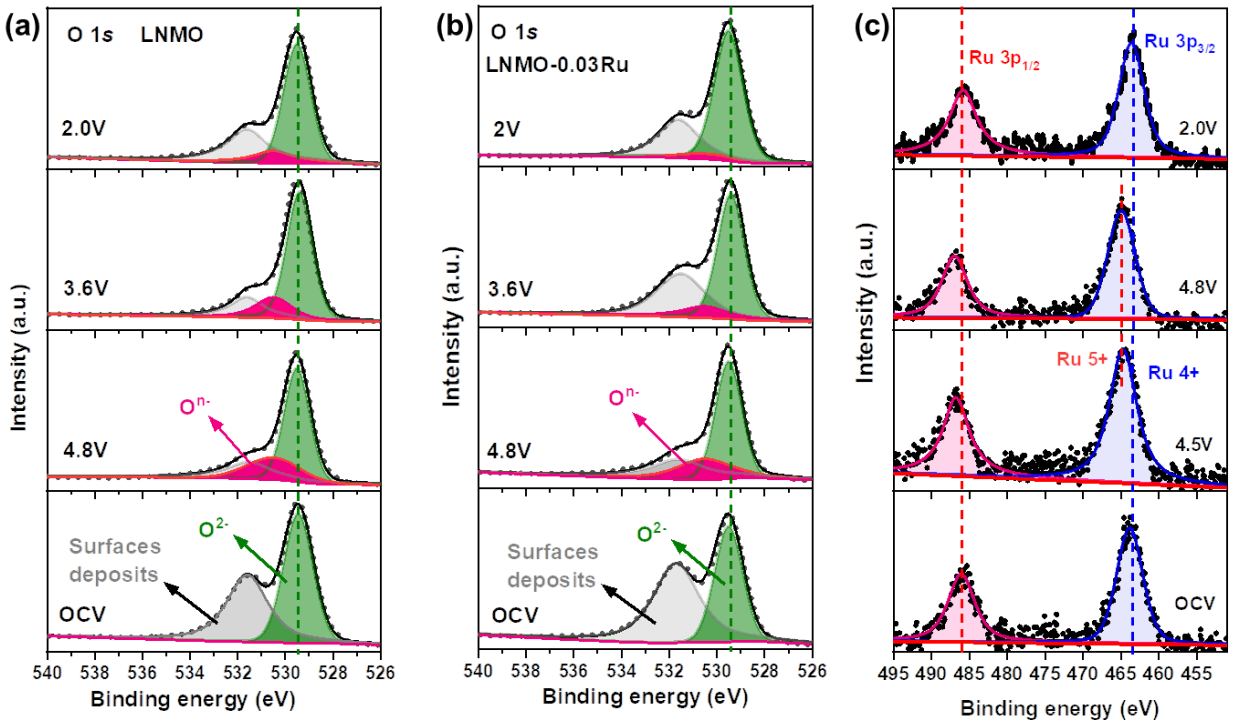

Figure S8. O 1*s* XPS spectra of the (a) undoped LNMO and (b) LNMO-0.03Ru at the OCV, fully charged, discharged to 3.6 V, and fully discharged state; (c) Ru 3*p* XPS spectra of LNMO-0.03Ru at different charge/discharge states.

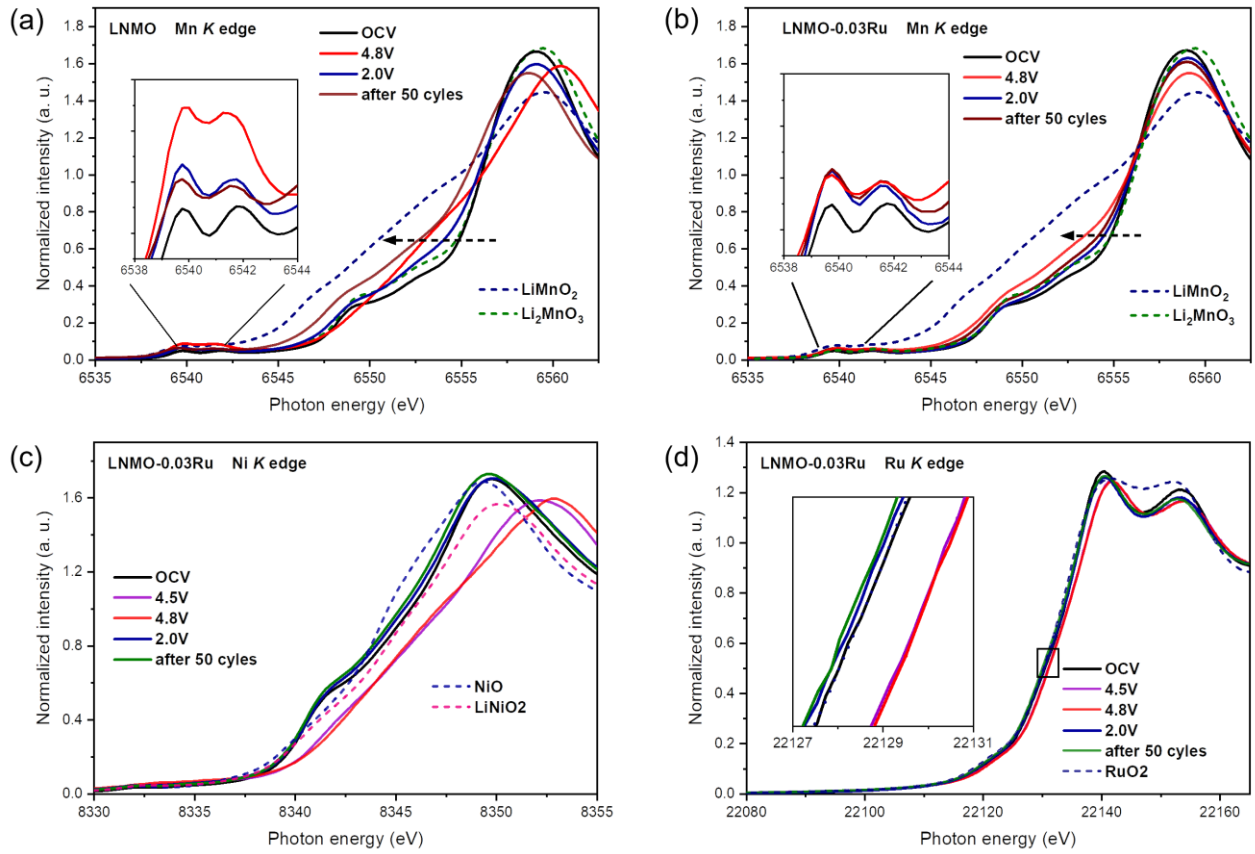

Figure S9. Mn K edge of (a) LNMO and (b) LNMO-0.03Ru; (c) Ni K edge of LNMO and LNMO-0.03Ru; (d) Ru K edge of LNMO-0.03Ru.

X-ray absorption near-edge spectroscopy (XAS) was employed in transmission mode to explore the bulk oxidation state and coordination of Mn and Ni of electrodes at various SOCs. Figure S11c shows the XAS of Mn at OCV, fully charged (4.8V), fully discharged (2.0V), and the discharged state after 50 cycles. As charged to 4.8 V, the Mn K-edge position of LNMO shifts toward lower energy (Figure S9a), suggesting a partial reduction of Mn^{4+} occurs at high potential, as reported elsewhere.[16] The distinct changes in Mn K-edge shape and increased pre-edge intensity can be attributed to dramatic variations in the local coordination.[17] Such changes in Mn over the first charge cycle are almost irreversible. Moreover, a further shift to lower energy was observed for that of the cycled LNMO, indicating the formation of bulk Mn^{2+} and Mn^{3+} during cycling. The reduction of Mn^{4+} is considerably inhibited in LNMO-0.03Ru (Figure S9b) though a slight shift of the Mn K-edge spectra for LNMO-0.03Ru could be due to a minor presence of Mn^{3+}.

The redox behaviour of Ni was investigated for LNMO and LNMO-0.03Ru during the first charge cycle and again after 50 cycles (Figure S9c). A similar evolution of Ni K edge was observed in LNMO and LNMO-0.03Ru. At OCV, Ni has a valence of 2+, whereas after charging to 4.5 V, Ni^{2+} is oxidized to Ni^{4+}, as evidenced by the positive edge shift (beyond the Ni^{3+} reference). No changes were found for the Ni K-edge when charged beyond 4.5 V. This suggests the oxidation to Ni^{4+} takes place before the 4.5 V plateau. It is fully recovered to the pristine state when discharging to 2.0 V and after cycling, manifesting the highly reversible $Ni^{2+/4+}$ redox process in bulk and eliminating the impact of $Ni^{2+/4+}$ redox on the capacity and voltage decay.

The Ru K-edge spectra of LNMO-0.03Ru are shown in Figure S9d. It reveals that the Ru participates in the charge compensation during electrochemical cycling and the Ru redox is fully reversible. At OCV, the valence of Ru is determined to be 4+ by comparison to a relevant Ru^{4+} reference (RuO_2). The Ru K edge shifts to higher energy upon charging to 4.5 V and shows no noticeable changes at the subsequent charge point (4.8 V). The energy shift of ~1.3 eV is in good agreement with an oxidation state change of Ru from 4+ to 5+.[18] Upon discharge, the Ru K edge shifts back to the initial energy point. This reversible Ru redox was further confirmed by XPS analysis of Ru 3*p* core spectra (Figure S8c). Overall, Ni^{2+} and Ru^{4+} participate in the charge compensation in LNMO-0.03Ru during charging and discharging, contributing to capacity as reversible cationic redox centres. Moreover, it is notable that the oxidation of Ru^{4+} occurs along with the O^{2-} reduction at the high voltage range. The appearance of Ru^{5+} at the time of O^{2-} deficiency can be an asset in strengthening the lattice structure.

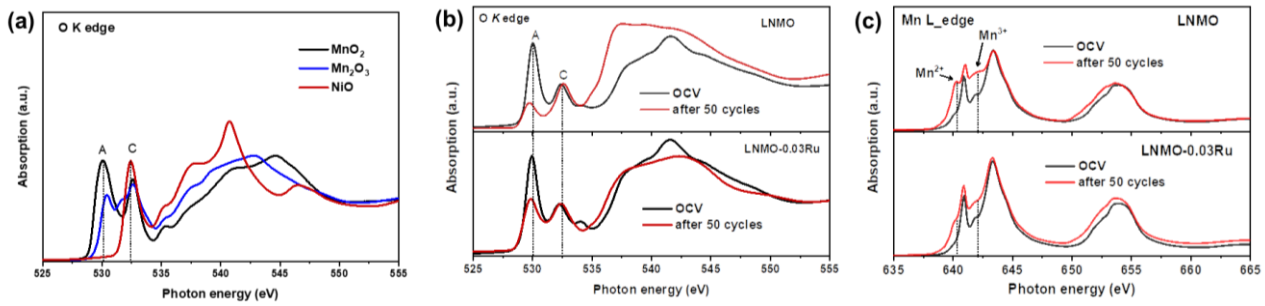

Figure S10. O K edge NEXAFS spectra of (a) the samples for reference, including MnO_2, Mn_2O_3, and NiO, and (b) the undoped LNMO and LNMO-0.03Ru at the OCV and after 50 cycles; (c) Mn L edge NEXAFS spectra of the undoped LNMO and LNMO-0.03Ru at the OCV state and after 50 cycles.

After 50 cycles, the DOHS of LNMO decreases substantially (Figure S10b), as a result of the significantly reduced peak A that corresponds to the hybridization of O 2*p* and Mn 3*d* orbitals. The reduction of peak A implies the loss of surface Mn (Figure S10a), reflecting the occurrence of Mn dissolution in LNMO. In contrast, the loss of Mn in LNMO-0.03Ru is less significant. It is noted that the intensity of peak C, which relates to the hybridization of O 2*p* and Ni 3*d* orbitals, remains unchanged over 50 cycles, which is further supported by the high reversibility of Ni K-edge spectra for LNMO and LNMO-0.03Ru (Figure S9c), ruling out the impact of $Ni^{2+/4+}$ redox on the capacity and voltage decay. More importantly, this finding unambiguously suggests that the higher capacity and voltage retention for LNMO-0.03Ru is attributed to enhanced oxygen lattice.

The amount of Mn^{2+} and Mn^{3+} in LNMO-0.03Ru is still relatively lower than in LNMO after 50 cycles (Figure S10c). These results concur with O K-edge analysis that the Mn dissolution can be mitigated by Ru doping, showing excellent agreement with the *in operando* XRPD results in a more robust O lattice and better cycling stability in LNMO-0.03Ru.

SUPPORTING INFORMATION

To probe the energetic stability of ruthenium in LNMO and its effect on the oxygen lattice, a set of substitutional doping DFT simulations were performed based on the experimentally measured structures in Table S1 and S2. For m-LNMO, there is no nickel in the structure; hence, only one configuration needs to be considered. The optimized structure of m-LNMO had an antiferromagnetic (AFM) ground state with an Mn magnetic moment of 3.2 μ_B and a band gap of 2.44 eV. For h-LNMO, we conducted cell optimizations on 2×2×1 expansion of the hexagonal cell in Table S7. The cell expansion and generation of the inequivalent h-LNMO structures were conducted using the supercell programme,[19] resulting in a total of eleven inequivalent h-LNMO structures, which were ranked energetically after optimization to obtain the lowest energy structures. Four of these structures were within k_BT at room temperature and were used to study the Ru doping (Figure S11). In real systems, the h-LNMO configurations would be expected to be coexistent due to their similar energetic stability. All configurations have AFM ordering on the TM ions, with Ni magnetic moments of 1.8 μ_B and mixed Mn magnetic moments of 3.3 μ_B and 3.9 μ_B. Substitution of one Ru on an Mn (Ru_{Mn}) site was conducted in the lowest h-LNMO configurations, and each structure geometry was optimized. This resulted in a total of 12 inequivalent dopant sites for each h-LNMO structure and eight for m-LNMO.

From DFT simulations, the location of Ru dopants and their impact on the oxygen lattice was probed through their defect formation energies ($E_f(j)$). ($E_f(j)$) was calculated for Ru doping on Mn sites and subsequent oxygen vacancy (V_O) formation through the following expression:[20]

$$E_f(j) = E_D - E_{Bulk} + \sum n_i \mu_i \quad \text{(eq. 1)}$$

Here j is the investigated defect (that is Ru_{TM} for Ru doping on a transition metal site, or V_O for oxygen vacancy using the Kröger-Vink notation[21]), E_D is the total energy of the system with j, E_{bulk} is the total energy of the reference bulk system, i is the species that have either been added or removed to recreate the defect, n_i is the number of i species, and μ_i is the chemical potential of species i. μ_{Ru}, μ_{Ni}, and μ_{Mn} were calculated from their metallic bulks, whereas μ_O was taken as half the total energy of an O_2 molecule in the triplet state.[22] The resulting $E_f(Ru_{TM})$ values are presented in Figure S12, and further data are provided in Table S7, S8, and S9. $E_f(Ru_{TM})$ values in the two phases are quite close, demonstrating the possibility of two-phase doping.

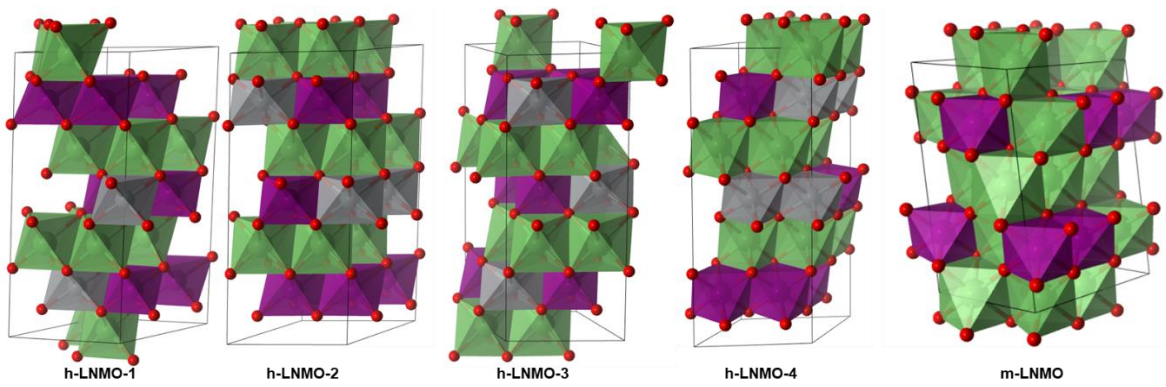

Figure S11. Polyhedral view of the optimized lowest energy configurations of h-LNMO and m-LNMO. The labelling refers to the ones used in Table S7. Green signifies Li, purple Mn, grey Ni, and red O. All structural figures were made using VESTA.[23]

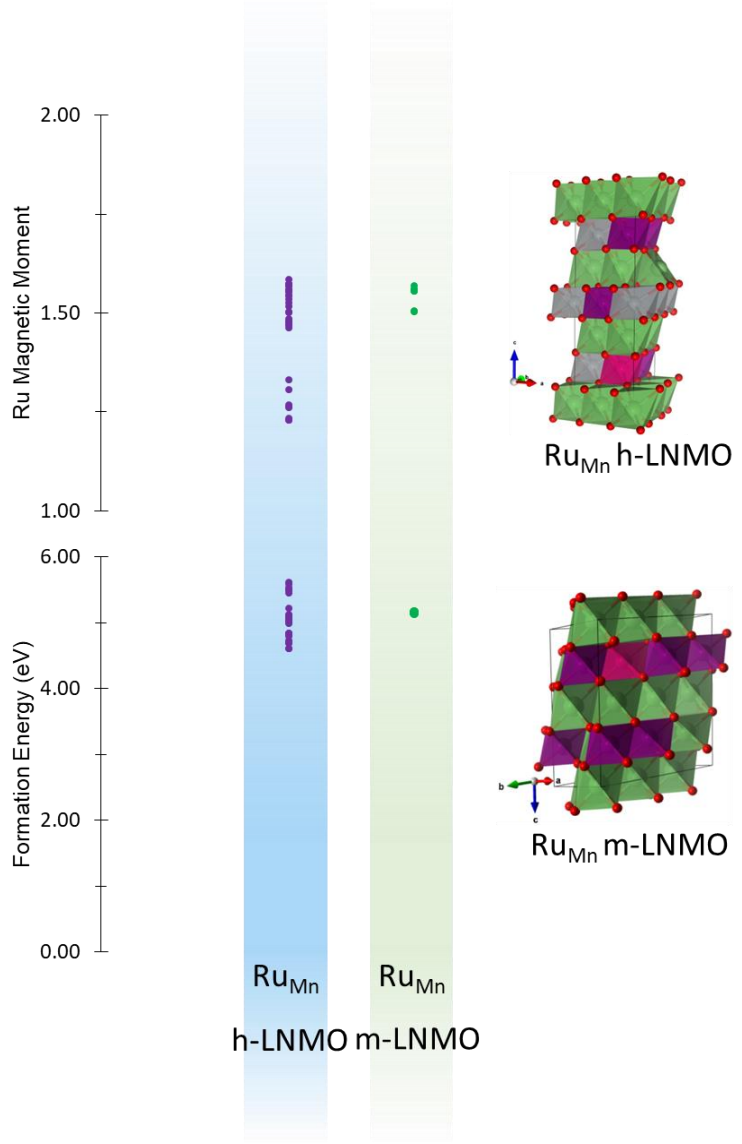

Figure S12. Ru magnetic moments and Ru_{Mn} formation energies plotted for each Ru site in h-LNMO. Insets show polyhedral representations of optimized Ru_{Mn} systems. Li positions are shown in green, Ni in grey, Mn in purple, Ru in pink, and O in red.

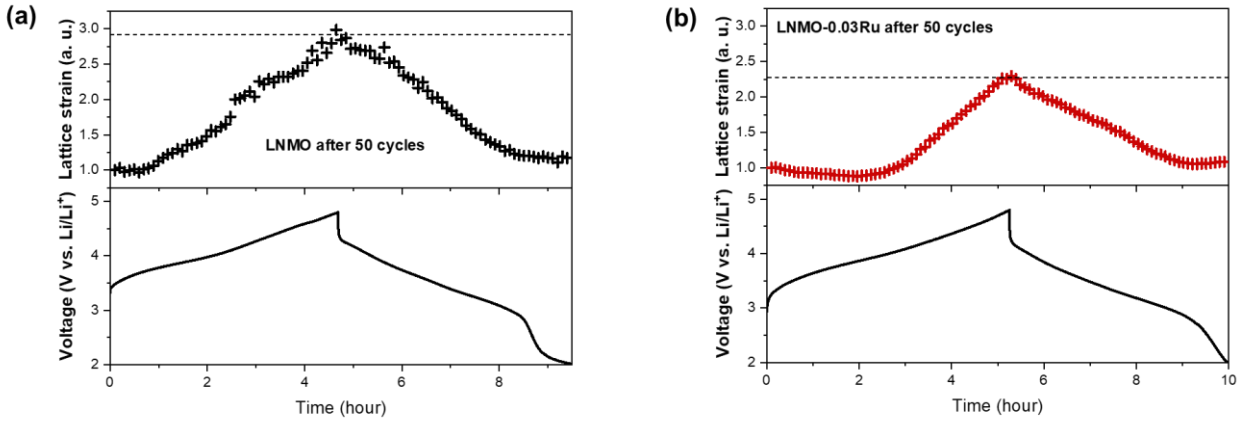

Figure S13. The estimated lattice strain and corresponding electrochemical voltage curves of (a) LNMO after 50 cycles and (b) LNMO-0.03Ru after 50 cycles.

According to Williamson-Hall's method, lattice strain (Ɛ) depends on not only crystallite sizes (related to peak position 2θ) but also peak broadening (peak width at half-maximum).[35] Lattice strain can be calculated using the formula below:

lattice strain $\varepsilon = \frac{\beta_{hkl}}{4\tan\theta}$,

where the β_{hkl} is the width of the half-maximum intensity of instrumental corrected broadening.[35]

SUPPORTING INFORMATION

Table S1. Phase composition and crystallography details of undoped LNMO obtained from joint Rietveld refinement using NPD and XRPD data.

LNMO							
Phase1	**Hexagonal *R*-3*m* phase (40(2) wt%)**						
	***a*/Å**			***c*/Å**		**Volume/Å^3**	
	2.8614(1)			14.252(6)		101.067(6)	
	Mn-O bond length/Å						
	1.9707(21) (BVS = +3.33)						
	Atom	**Wyckoff site**	***x***	***y***	***z***	**U_{iso} (Å^2)**	**Site occupancy factor**
	Li1	3*b*	0	0	0	0.08743	0.9870
	Ni1	3*b*	0	0	0	0.08743	0.0130
	Li2	3*a*	0	0	0.5	0.03283	0.0296
	Ni2	3*a*	0	0	0.5	0.03283	0.3469
	Mn1	3*a*	0	0	0.5	0.03283	0.6235
	O	6*c*	0	0	0.24209	0.03779	1.0000
Phase2	**Monoclinic *C*2/*c* phase (60(2) wt%)**						
	***a*/Å**	***b*/Å**		***c*/Å**	**beta/^{o}**	**Volume/Å^3**	
	4.9572(4)	8.5763(3)		9.638(1)	99.646(3)	403.97(2)	
	Mn1-O bond length/Å						
	2.060(4)	2.148(7)		1.993(6)		BVS = +2.62	
	Mn2-O bond length/Å						
	1.926(9)	1.856(9)		1.893(7)		BVS = +4.14	
	Mn3-O bond length/Å						
	1.973(8)	1.952(6)		1.921(7)		BVS = +3.54	
	Atom	**Wyckoff site**	***x***	***y***	***z***	**U_{iso} (Å^2)**	**Site occupancy factor**
	Li1	8*f*	0.22732	0.08538	-0.00652	0.00552	1.0000
	Li2	4*d*	0.25	0.25	0.5	0.01205	1.0000
	Li3	4*e*	0	0.76349	0.25	0.09675	0.6087
	Mn1	4*e*	0	0.76349	0.25	0.09675	0.3913
	Mn2	4*e*	0	0.42092	0.25	0.01461	1.0000
	Mn3	4*e*	0	0.07652	0.25	0.12703	0.8817
	Li5	4*e*	0	0.07652	0.25	0.12703	0.1183
	O1	8*f*	0.10741	0.25235	0.13892	0.00379	1.0000
	O2	8*f*	0.13334	0.56897	0.13843	0.01043	1.0000
	O3	8*f*	0.14970	0.92609	0.13612	0.00130	1.0000

SUPPORTING INFORMATION

Table S2. Phase composition and crystallography details of LNMO-0.03Ru obtained from joint Rietveld refinement using NPD and XRPD data.

LNMO-0.03Ru							
Phase1	Hexagonal *R*-3*m* phase (52(1) wt%)						
	***a*/Å**			***c*/Å**		**Volume/Å^3**	
	2.8644(1)			14.2621(8)		101.345(8)	
	Mn-O bond length/Å						
	1.9751(24) (BVS = +3.29)						
	Atom	**Wyckoff site**	***x***	***y***	***z***	**U_{iso} (Å^2)**	**Site occupancy factor**
	Li1	3*b*	0	0	0	0.07078	0.9870
	Ni1	3*b*	0	0	0	0.07078	0.0130
	Li2	3*a*	0	0	0.5	0.02775	0.0296
	Ni2	3*a*	0	0	0.5	0.02775	0.3469
	Mn1	3*a*	0	0	0.5	0.02775	0.6235
	O	6*c*	0	0	0.24239	0.02408	1.0000
Phase2	Monoclinic *C*2/*c* phase (48 (1) wt%)						
	***a*/Å**		***b*/Å**	***c*/Å**	**beta/^{o}**	**Volume/Å^3**	
	4.961(1)		8.572(7)	9.644(3)	99.75(1)	404.27(4)	
	Mn1-O bond length/Å						
	2.069(8)		2.049(9)	2.173(8)		BVS = +2.39	
	Mn2-O bond length/Å						
	1.908(13)		1.833(12)	1.891(9)		BVS = +4.30	
	Mn3-O bond length/Å						
	2.047(17)		1.975(9)	1.859(14)		BVS = +3.50	
	Atom	**Wyckoff site**	***x***	***y***	***z***	**U_{iso} (Å^2)**	**Site occupancy factor**
	Li1	8*f*	0.26231	0.08348	0.00467	-0.00833	1.0000
	Li2	4*d*	0.25	0.25	0.5	0.01693	1.0000
	Li3	4*e*	0	0.73462	0.25	0.01288	0.6087
	Mn1	4*e*	0	0.73462	0.25	0.01288	0.3913
	Mn2	4*e*	0	0.42298	0.25	0.02709	1.0000
	Mn3	4*e*	0	0.06514	0.25	0.14651	0.8817
	Li5	4*e*	0	0.06514	0.25	0.14651	0.1183
	O1	8*f*	0.10454	0.25453	0.14127	0.00896	1.0000
	O2	8*f*	0.13296	0.56048	0.13257	0.02550	1.0000
	O3	8*f*	0.14988	0.92594	0.13635	0.00178	1.0000

Table S3. Capacity retention and voltage decay comparison of LNMO-0.03Ru with other previously reported Co-free LLOs.

Cathode Material	Current rate	Capacity (mAh g^{-1})	Cycles	Capacity Retention	Voltage Decay per cycle (mV)	Ref.
Gas-treated $Li_{1.2}Ni_{0.2}Mn_{0.6}O_2$	1 C	200	200	77.2%	1.95	[24]
Li_2SiO_3-coated $Li_{1.13}Ni_{0.3}Mn_{0.57}O_2$	1 C	165	100	90%	1.92	[25]
Nb-doped $Li_{1.2}Ni_{0.27}Mn_{0.53}O_2$	1 C	212	200	86%	1.89	[26]
Urea-treated $Li_{1.87}Ni_{0.19}Mn_{0.94}O_3$	0.1 C	250	300	100%	1.88	[27]
Surface modified- $Li_{1.2}Ni_{0.2}Mn_{0.6}O_2$	1 C	210	200	91%	1.77	[28]
AlF_3-coated $Li_{1.2}Ni_{0.2}Mn_{0.6}O_2$	300 mA g^{-1}	200	100	88%	1.40	[29]
Surface-modified $Li_{1.2}Ni_{0.2}Mn_{0.6}O_2$	1 C	250	500	90%	1.09	[30]
Porous $Li_{1.17}Ni_{0.25}Mn_{0.58}O_2$	0.5 C	231	200	94%	0.90	[31]
$Li_{1.2}Mn_{0.585}Ni_{0.185}Fe_{0.03}O_2$	1 C	160	200	80%	0.85	[32]
$LiMn_{0.8}Fe_{0.2}PO_4$/C-blended $Li_{1.2}Ni_{0.2}Mn_{0.6}O_2$	1 C	160	500	80%	0.71	[33]
Zr-doped $Li_{1.2}Ni_{0.2}Mn_{0.6}O_2$	1 C	180	300	92%	0.45	[34]
LNMO-0.03Ru	**1 C**	**215**	**200**	**93%**	**< 0.45**	**This work**
			300	**90%**		
			500	**74%**		

Table S4. ICP-AES analysis data for the atomic compositions of LNMO and LNMO-0.03Ru.

Sample	Measured Atomic ratio			
	Li	**Mn**	**Ni**	**Ru**
LNMO	0.61(1)	0.29(1)	0.09(1)	\
LNMO-0.03Ru	0.61(1)	0.28(1)	0.09(1)	0.014(1)
LNMO after 50 cycles	0.68(1)	0.24(1)	0.08(1)	\
LNMO-0.03Ru after 50 cycles	0.63(1)	0.27(1)	0.08(1)	0.013(1)

* Excess Li in the cycled electrodes may come from the electrolyte or anode during cell disassembly.

SUPPORTING INFORMATION

Table S5. The lattice parameter and corresponding errors, as obtained from single peak fitting of the *operando* XRPD data for LNMO and LNMO-0.03Ru.

LNMO				LNMO-0.03Ru			
a/Å	error/Å	c/Å	error/Å	a/Å	error/Å	c/Å	error/Å
4.9431	0.0001	9.6323	0.0001	4.9736	0.0002	9.6304	0.0002
4.9451	0.0003	9.6371	0.0001	4.9739	0.0002	9.6307	0.0002
4.9440	0.0003	9.6375	0.0001	4.9733	0.0001	9.6298	0.0002
4.9420	0.0003	9.6389	0.0001	4.9723	0.0001	9.6300	0.0001
4.9412	0.0002	9.6412	0.0001	4.971	0.0001	9.6302	0.0001
4.9397	0.0003	9.6420	0.0001	4.9698	0.0001	9.6308	0.0001
4.9386	0.0003	9.6434	0.0001	4.9687	0.0001	9.6304	0.0002
4.9380	0.0002	9.6447	0.0001	4.9683	0.0001	9.6310	0.0002
4.9372	0.0002	9.6461	0.0001	4.9674	0.0001	9.6319	0.0002
4.9367	0.0002	9.6477	0.0002	4.9657	0.0002	9.6324	0.0002
4.9363	0.0002	9.6490	0.0002	4.9653	0.0002	9.6332	0.0002
4.9355	0.0001	9.6503	0.0003	4.9645	0.0002	9.6333	0.0002
4.9351	0.0003	9.6518	0.0003	4.9638	0.0002	9.6350	0.0002
4.9344	0.0002	9.6531	0.0004	4.9631	0.0002	9.6350	0.0002
4.9337	0.0002	9.6538	0.0004	4.9622	0.0002	9.6350	0.0002
4.9332	0.0002	9.6549	0.0005	4.9615	0.0002	9.6355	0.0002
4.9327	0.0002	9.6556	0.0005	4.9608	0.0002	9.6360	0.0002
4.9319	0.0001	9.6571	0.0006	4.9604	0.0002	9.6361	0.0002
4.9307	0.0001	9.6578	0.0006	4.9599	0.0002	9.6366	0.0002
4.9300	0.0001	9.6599	0.0007	4.9596	0.0002	9.6371	0.0002
4.9288	0.0001	9.6611	0.0007	4.9586	0.0002	9.6378	0.0002
4.9274	0.0001	9.6648	0.0008	4.9583	0.0001	9.6389	0.0002
4.9262	0.0001	9.6672	0.0008	4.9576	0.0001	9.6390	0.0002
4.9250	0.0001	9.6707	0.0007	4.9571	0.0001	9.6399	0.0002
4.9234	0.0001	9.6736	0.0007	4.9564	0.0001	9.6410	0.0002
4.9220	0.0001	9.6783	0.0005	4.9558	0.0001	9.6417	0.0002
4.9204	0.0001	9.6812	0.0004	4.9552	0.0001	9.6423	0.0002
4.9186	0.0001	9.6844	0.0003	4.9551	0.0001	9.6426	0.0002
4.9172	0.0001	9.6871	0.0002	4.9554	0.0001	9.6433	0.0002
4.9162	0.0001	9.6896	0.0003	4.9542	0.0001	9.6439	0.0002
4.9152	0.0001	9.6917	0.0003	4.9532	0.0001	9.6447	0.0002
4.9144	0.0001	9.6933	0.0005	4.9526	0.0001	9.6467	0.0002
4.9137	0.0001	9.6951	0.0005	4.9519	0.0001	9.6469	0.0003
4.9133	0.0001	9.6966	0.0005	4.9516	0.0001	9.6477	0.0002
4.9124	0.0001	9.6975	0.0006	4.9512	0.0001	9.6484	0.0002
4.9118	0.0001	9.6997	0.0006	4.9504	0.0001	9.6492	0.0002
4.9118	0.0001	9.7005	0.0007	4.9493	0.0001	9.6501	0.0002
4.9116	0.0001	9.7012	0.0007	4.9488	0.0001	9.6510	0.0003
4.9114	0.0001	9.7022	0.0007	4.9481	0.0001	9.6523	0.0003
4.9110	0.0001	9.7028	0.0007	4.9477	0.0001	9.6532	0.0003
4.9109	0.0001	9.7033	0.0007	4.9469	0.0001	9.6543	0.0003
4.9106	0.0001	9.7039	0.0008	4.9466	0.0001	9.6553	0.0003
4.9104	0.0001	9.7041	0.0007	4.9455	0.0001	9.6565	0.0003

4.9103	0.0001	9.7045	0.0007	4.9448	0.0001	9.6583	0.0003
4.9102	0.0001	9.7047	0.0008	4.9434	0.0001	9.6597	0.0003
4.9101	0.0002	9.7048	0.0008	4.9426	0.0001	9.6614	0.0003
4.9102	0.0002	9.7056	0.0008	4.9418	0.0001	9.6631	0.0003
4.9100	0.0002	9.7055	0.0008	4.9412	0.0001	9.6651	0.0003
4.9097	0.0002	9.7055	0.0007	4.9395	0.0001	9.6666	0.0003
4.9097	0.0002	9.7054	0.0007	4.9385	0.0001	9.6684	0.0003
4.9095	0.0002	9.7053	0.0007	4.9372	0.0001	9.6712	0.0003
4.9096	0.0002	9.7058	0.0007	4.9361	0.0001	9.6738	0.0004
4.9095	0.0002	9.7060	0.0007	4.9347	0.0001	9.6757	0.0003
4.9095	0.0001	9.7062	0.0008	4.934	0.0001	9.6788	0.0003
4.9096	0.0001	9.7065	0.0007	4.9329	0.0001	9.6808	0.0004
4.9092	0.0001	9.7061	0.0007	4.932	0.0001	9.6832	0.0003
4.9090	0.0001	9.7061	0.0008	4.9313	0.0001	9.6845	0.0004
4.9091	0.0001	9.7067	0.0008	4.9314	0.0001	9.6874	0.0004
4.9089	0.0001	9.7067	0.0007	4.9308	0.0001	9.6885	0.0004
4.9088	0.0001	9.7074	0.0008	4.9305	0.0002	9.6900	0.0003
4.9088	0.0001	9.7078	0.0008	4.9298	0.0003	9.6918	0.0004
4.9086	0.0001	9.7079	0.0008	4.9295	0.0003	9.6954	0.0004
4.9086	0.0001	9.7078	0.0008	4.9285	0.0003	9.6970	0.0004
4.9088	0.0001	9.7082	0.0009	4.9287	0.0004	9.6983	0.0004
4.9088	0.0001	9.7080	0.0008	4.9279	0.0006	9.6997	0.0005
4.9090	0.0000	9.7082	0.0009	4.9275	0.0005	9.7004	0.0005
4.9093	0.0001	9.7089	0.0008	4.9277	0.0005	9.7012	0.0004
4.9089	0.0001	9.7080	0.0008	4.9272	0.0002	9.7021	0.0005
4.9089	0.0001	9.7080	0.0009	4.927	0.0001	9.7026	0.0005
4.9093	0.0001	9.7086	0.0009	4.9269	0.0001	9.7028	0.0005
4.9093	0.0001	9.7075	0.0008	4.9267	0.0001	9.7039	0.0005
4.9095	0.0001	9.7073	0.0008	4.9268	0.0001	9.7042	0.0005
4.9097	0.0001	9.7074	0.0008	4.9268	0.0001	9.7049	0.0005
4.9101	0.0001	9.7073	0.0008	4.9265	0.0001	9.7050	0.0005
4.9103	0.0001	9.7068	0.0008	4.9262	0.0001	9.7056	0.0005
4.9105	0.0001	9.7063	0.0008	4.9257	0.0001	9.7062	0.0005
4.9105	0.0001	9.7054	0.0008	4.9256	0.0001	9.7061	0.0005
4.9108	0.0001	9.7048	0.0008	4.9256	0.0001	9.7063	0.0005
4.9110	0.0001	9.7037	0.0008	4.9257	0.0001	9.7062	0.0005
4.9115	0.0001	9.7036	0.0007	4.9254	0.0001	9.7066	0.0005
4.9115	0.0001	9.7019	0.0007	4.9256	0.0001	9.7062	0.0005
4.9118	0.0001	9.7014	0.0007	4.9252	0.0001	9.7065	0.0005
4.9122	0.0001	9.7012	0.0007	4.925	0.0001	9.7071	0.0005
4.9124	0.0001	9.7001	0.0007	4.9253	0.0001	9.7073	0.0005
4.9126	0.0001	9.6994	0.0007	4.9252	0.0001	9.7067	0.0005
4.9131	0.0001	9.6987	0.0006	4.9245	0.0001	9.7071	0.0005
4.9135	0.0001	9.6979	0.0007	4.925	0.0001	9.7066	0.0006
4.9140	0.0001	9.6971	0.0006	4.9248	0.0001	9.7067	0.0005
4.9144	0.0001	9.6958	0.0006	4.9247	0.0001	9.7065	0.0005

4.9149	0.0002	9.6942	0.0005	4.9243	0.0000	9.7065	0.0005
4.9155	0.0002	9.6927	0.0006	4.9245	0.0000	9.7065	0.0005
4.9164	0.0002	9.6916	0.0005	4.9243	0.0000	9.7057	0.0005
4.9172	0.0002	9.6901	0.0005	4.9248	0.0000	9.7071	0.0005
4.9181	0.0002	9.6892	0.0005	4.9247	0.0000	9.7064	0.0005
4.9190	0.0002	9.6871	0.0004	4.9248	0.0000	9.7064	0.0005
4.9197	0.0002	9.6846	0.0004	4.925	0.0000	9.7064	0.0005
4.9209	0.0002	9.6828	0.0004	4.9245	0.0000	9.7068	0.0005
4.9218	0.0002	9.6803	0.0003	4.9252	0.0000	9.7068	0.0005
4.9228	0.0002	9.6787	0.0003	4.9253	0.0000	9.7065	0.0005
4.9239	0.0002	9.6760	0.0003	4.9251	0.0000	9.7057	0.0005
4.9248	0.0001	9.6734	0.0002	4.9252	0.0000	9.7065	0.0005
4.9259	0.0001	9.6713	0.0002	4.9252	0.0000	9.7065	0.0005
4.9271	0.0001	9.6689	0.0002	4.9254	0.0000	9.7065	0.0005
4.9282	0.0001	9.6658	0.0002	4.9253	0.0001	9.7067	0.0005
4.9293	0.0001	9.6621	0.0002	4.9255	0.0001	9.7066	0.0005
4.9306	0.0001	9.6583	0.0002	4.9255	0.0001	9.7071	0.0005
4.9323	0.0002	9.6548	0.0002	4.9255	0.0001	9.7067	0.0005
4.9344	0.0002	9.6519	0.0002	4.9258	0.0001	9.7072	0.0005
4.9358	0.0002	9.6488	0.0002	4.926	0.0001	9.7070	0.0005
--		--		4.9262	0.0001	9.7065	0.0005
--		--		4.9262	0.0001	9.7063	0.0005
--		--		4.9262	0.0001	9.7066	0.0005
--		--		4.9263	0.0001	9.7063	0.0005
--		--		4.9264	0.0001	9.7064	0.0005
--		--		4.9265	0.0001	9.7062	0.0005
--		--		4.9266	0.0001	9.7063	0.0005
--		--		4.9268	0.0001	9.7058	0.0005
--		--		4.9268	0.0001	9.7053	0.0005
--		--		4.9271	0.0001	9.7052	0.0005
--		--		4.9275	0.0001	9.7047	0.0005
--		--		4.9278	0.0001	9.7044	0.0005
--		--		4.9281	0.0001	9.7044	0.0005
--		--		4.9285	0.0001	9.7043	0.0005
--		--		4.9289	0.0001	9.7033	0.0005
--		--		4.9292	0.0001	9.7022	0.0005
--		--		4.9297	0.0001	9.7016	0.0005
--		--		4.9298	0.0001	9.7003	0.0005
--		--		4.9303	0.0001	9.6992	0.0005
--		--		4.9308	0.0001	9.6989	0.0005
--		--		4.9314	0.0001	9.6979	0.0005
--		--		4.9318	0.0001	9.6968	0.0005
--		--		4.9324	0.0001	9.6950	0.0005
--		--		4.9332	0.0001	9.6939	0.0005
--		--		4.9333	0.0001	9.6931	0.0006
--		--		4.9342	0.0001	9.6921	0.0005

--		--		4.9345	0.0001	9.6911	0.0005
--		--		4.9349	0.0001	9.6898	0.0005
--		--		4.9354	0.0001	9.6888	0.0005
--		--		4.936	0.0001	9.6876	0.0005
--		--		4.9364	0.0002	9.6865	0.0005
--		--		4.9372	0.0002	9.6844	0.0005
--		--		4.938	0.0001	9.6821	0.0005
--		--		4.9384	0.0001	9.6813	0.0005
--		--		4.9393	0.0002	9.6789	0.0005
--		--		4.9397	0.0002	9.6778	0.0005
--		--		4.941	0.0002	9.6764	0.0005
--		--		4.9416	0.0002	9.6753	0.0005
--		--		4.942	0.0002	9.6737	0.0006
--		--		4.9428	0.0002	9.6729	0.0005
--		--		4.9438	0.0002	9.6711	0.0005
--		--		4.9444	0.0002	9.6704	0.0005
--		--		4.9457	0.0002	9.6694	0.0005
--		--		4.9463	0.0002	9.6677	0.0005
--		--		4.9473	0.0002	9.6665	0.0005
--		--		4.9484	0.0002	9.6648	0.0005
--		--		4.9495	0.0002	9.6627	0.0004
--		--		4.9512	0.0002	9.6626	0.0003
--		--		4.9526	0.0002	9.6603	0.0002
--		--		4.9531	0.0002	9.6588	0.0002
--		--		4.9542	0.0002	9.6564	0.0002
--		--		4.9546	0.0002	9.6535	0.0002
--		--		4.9553	0.0002	9.6500	0.0002
--		--		4.9556	0.0002	9.6479	0.0002
--		--		4.9561	0.0002	9.6448	0.0002
--		--		4.956	0.0002	9.6435	0.0002
--		--		4.9558	0.0002	9.6433	0.0002

SUPPORTING INFORMATION

Table S6. The lattice parameter and corresponding errors, as obtained from single peak fitting of the operando XRPD data for the cycled LNMO and LNMO-0.03Ru.

LNMO after 50 cycles				LNMO-0.03Ru after 50 cycles			
a/Å	error/Å	c/Å	error/Å	a/Å	error/Å	c/Å	error/Å
2.8687	0.0003	14.3544	0.0016	2.8755	0.0001	14.3225	0.0014
2.8677	0.0003	14.3551	0.0016	2.8759	0.0001	14.3211	0.0014
2.8669	0.0003	14.3538	0.0016	2.8747	0.0002	14.3211	0.0013
2.8662	0.0003	14.3542	0.0016	2.8736	0.0001	14.3211	0.0013
2.8657	0.0003	14.3547	0.0014	2.8727	0.0001	14.3227	0.0013
2.8651	0.0003	14.3545	0.0016	2.8718	0.0001	14.3229	0.0012
2.8643	0.0003	14.3555	0.0015	2.8710	0.0001	14.3232	0.0011
2.8637	0.0003	14.3558	0.0015	2.8701	0.0001	14.3229	0.0011
2.8630	0.0003	14.3560	0.0014	2.8694	0.0002	14.3226	0.0011
2.8621	0.0003	14.3574	0.0014	2.8688	0.0002	14.3226	0.0010
2.8616	0.0003	14.3586	0.0012	2.8684	0.0002	14.3208	0.0009
2.8606	0.0002	14.3610	0.0013	2.8680	0.0002	14.3208	0.0009
2.8598	0.0003	14.3626	0.0013	2.8676	0.0002	14.3209	0.0009
2.8589	0.0003	14.3658	0.0013	2.8670	0.0002	14.3204	0.0009
2.8576	0.0003	14.3711	0.0013	2.8666	0.0002	14.3199	0.0008
2.8565	0.0003	14.3741	0.0015	2.8660	0.0002	14.3192	0.0008
2.8551	0.0002	14.3788	0.0015	2.8654	0.0002	14.3205	0.0008
2.8537	0.0003	14.3843	0.0017	2.8648	0.0002	14.3209	0.0008
2.8524	0.0003	14.3917	0.0019	2.8643	0.0002	14.3211	0.0008
2.8513	0.0002	14.3987	0.0026	2.8637	0.0002	14.3217	0.0007
2.8497	0.0002	14.4072	0.0030	2.8629	0.0002	14.3230	0.0008
2.8484	0.0001	14.4158	0.0040	2.8623	0.0002	14.3242	0.0007
2.8459	0.0000	14.4269	0.0050	2.8616	0.0002	14.3264	0.0008
2.8440	0.0001	14.4362	0.0063	2.8609	0.0002	14.3288	0.0008
2.8416	0.0002	14.4437	0.0077	2.8600	0.0002	14.3306	0.0007
2.8393	0.0003	14.4628	0.0086	2.8591	0.0002	14.3332	0.0007
2.8376	0.0003	14.4635	0.0082	2.8581	0.0002	14.3367	0.0008
2.8362	0.0002	14.4783	0.0074	2.8571	0.0001	14.3397	0.0009
2.8351	0.0002	14.4799	0.0066	2.8560	0.0001	14.3432	0.0010
2.8335	0.0001	14.4816	0.0062	2.8548	0.0001	14.3470	0.0012
2.8332	0.0001	14.4774	0.0061	2.8534	0.0001	14.3514	0.0012
2.8324	0.0001	14.4756	0.0057	2.8521	0.0001	14.3549	0.0013
2.8319	0.0001	14.4720	0.0054	2.8506	0.0001	14.3578	0.0015
2.8314	0.0001	14.4669	0.0055	2.8491	0.0000	14.3626	0.0018
2.8312	0.0001	14.4619	0.0055	2.8475	0.0000	14.3658	0.0017
2.8311	0.0000	14.4566	0.0050	2.8461	0.0000	14.3688	0.0021
2.8310	0.0000	14.4510	0.0049	2.8450	0.0000	14.3695	0.0021
2.8309	0.0001	14.4459	0.0050	2.8434	0.0000	14.3701	0.0022
2.8309	0.0000	14.4428	0.0045	2.8423	0.0000	14.3701	0.0024
2.8309	0.0001	14.4382	0.0044	2.8413	0.0000	14.3676	0.0023
2.8307	0.0001	14.4334	0.0045	2.8406	0.0001	14.3636	0.0022

2.8302	0.0001	14.4282	0.0043	2.8401	0.0001	14.3607	0.0023
2.8296	0.0000	14.4222	0.0045	2.8400	0.0001	14.3563	0.0020
2.8294	0.0000	14.4200	0.0043	2.8393	0.0002	14.3516	0.0016
2.8305	0.0001	14.4138	0.0041	2.8393	0.0003	14.3469	0.0015
2.8304	0.0001	14.4108	0.0042	2.8389	0.0003	14.3422	0.0011
2.8296	0.0001	14.4089	0.0044	2.8385	0.0003	14.3367	0.0009
2.8302	0.0002	14.4090	0.0049	2.8382	0.0003	14.3311	0.0011
2.8309	0.0001	14.4241	0.0045	2.8380	0.0002	14.3271	0.0015
2.8313	0.0000	14.4404	0.0046	2.8377	0.0002	14.3208	0.0016
2.8321	0.0001	14.4543	0.0049	2.8371	0.0002	14.3195	0.0020
2.8325	0.0000	14.4676	0.0051	2.8369	0.0000	14.3163	0.0027
2.8326	0.0001	14.4822	0.0048	2.8369	0.0001	14.3107	0.0032
2.8337	0.0001	14.4869	0.0052	2.8366	0.0001	14.3079	0.0038
2.8346	0.0001	14.4908	0.0052	2.8373	0.0000	14.3104	0.0029
2.8356	0.0001	14.4885	0.0058	2.8382	0.0001	14.3221	0.0019
2.8363	0.0002	14.4888	0.0054	2.8389	0.0002	14.3302	0.0014
2.8377	0.0001	14.4860	0.0056	2.8397	0.0002	14.3361	0.0010
2.8392	0.0001	14.4824	0.0053	2.8408	0.0002	14.3399	0.0011
2.8408	0.0001	14.4757	0.0060	2.8416	0.0002	14.3447	0.0013
2.8419	0.0001	14.4723	0.0053	2.8426	0.0001	14.3466	0.0016
2.8432	0.0001	14.4669	0.0055	2.8430	0.0002	14.3504	0.0014
2.8445	0.0000	14.4612	0.0055	2.8442	0.0001	14.3482	0.0021
2.8458	0.0000	14.4532	0.0055	2.8450	0.0001	14.3504	0.0024
2.8472	0.0000	14.4466	0.0053	2.8460	0.0001	14.3501	0.0023
2.8487	0.0000	14.4414	0.0051	2.8471	0.0000	14.3507	0.0024
2.8498	0.0001	14.4385	0.0046	2.8480	0.0000	14.3500	0.0024
2.8514	0.0001	14.4310	0.0044	2.8491	0.0000	14.3493	0.0025
2.8526	0.0001	14.4235	0.0044	2.8499	0.0000	14.3489	0.0025
2.8543	0.0001	14.4151	0.0040	2.8508	0.0001	14.3477	0.0026
2.8553	0.0001	14.4097	0.0039	2.8520	0.0000	14.3460	0.0025
2.8569	0.0001	14.4045	0.0038	2.8529	0.0000	14.3449	0.0027
2.8582	0.0001	14.3982	0.0036	2.8539	0.0000	14.3433	0.0025
2.8593	0.0001	14.3942	0.0034	2.8548	0.0000	14.3414	0.0027
2.8607	0.0001	14.3886	0.0031	2.8560	0.0000	14.3401	0.0025
2.8618	0.0001	14.3850	0.0030	2.8570	0.0000	14.3386	0.0023
2.8630	0.0002	14.3812	0.0027	2.8580	0.0001	14.3367	0.0025
2.8638	0.0002	14.3780	0.0025	2.8590	0.0001	14.3353	0.0023
2.8649	0.0002	14.3753	0.0025	2.8599	0.0001	14.3341	0.0022
2.8654	0.0002	14.3743	0.0023	2.8609	0.0001	14.3327	0.0021
2.8664	0.0002	14.3709	0.0022	2.8618	0.0001	14.3306	0.0019
2.8672	0.0002	14.3704	0.0020	2.8626	0.0001	14.3288	0.0020
2.8681	0.0002	14.3706	0.0020	2.8633	0.0001	14.3286	0.0019
2.8691	0.0002	14.3684	0.0021	2.8643	0.0001	14.3260	0.0018
2.8704	0.0002	14.3681	0.0019	2.8649	0.0001	14.3264	0.0017
2.8717	0.0001	14.3688	0.0019	2.8656	0.0001	14.3250	0.0017
2.8723	0.0001	14.3697	0.0020	2.8664	0.0001	14.3247	0.0018

2.8728	0.0001	14.3705	0.0020	2.8670	0.0001	14.3241	0.0016
2.8733	0.0001	14.3725	0.0020	2.8676	0.0001	14.3237	0.0015
2.8734	0.0001	14.3722	0.0020	2.8685	0.0001	14.3246	0.0015
2.8738	0.0001	14.3712	0.0021	2.8694	0.0001	14.3245	0.0014
2.8741	0.0000	14.3709	0.0021	2.8704	0.0001	14.3245	0.0013
2.8745	0.0001	14.3676	0.0022	2.8714	0.0001	14.3247	0.0014
2.8748	0.0001	14.3692	0.0022	2.8725	0.0001	14.3255	0.0012
2.8752	0.0000	14.3672	0.0023	2.8739	0.0001	14.3262	0.0012
				2.8751	0.0001	14.3256	0.0011
				2.8762	0.0001	14.3278	0.0013
				2.8770	0.0002	14.3291	0.0012
				2.8776	0.0002	14.3309	0.0013
				2.8781	0.0002	14.3330	0.0011
				2.8784	0.0002	14.3351	0.0012

Table S7. The formation energies of substitutional Ru doping on transition metal sites. The values in the brackets denote multiple Ru_{TM} sites with the same formation energy. Where there are no brackets, only one site has this formation energy. The system naming system refers to that used in

12, with h signifying the hexagonal phase and m the monoclinic.

System	Lattice Vectors (Å)	E_g (eV)	Ru_{Mn} (eV)
h-LNMO-1	3.00, 2.92, 14.61	0.89	4.69, 4.73, 5.01, 5.03, 5.07, 5.08, 5.09, 5.11
h-LNMO-2	2.99, 3.01, 14.63	0.82	4.61 (×2), 4.71, 4.79, 4.83, 5.50, 5.53, 5.61
h-LNMO-3	3.01, 2.91, 14.64	0.91	4.84 (×2), 4.99, 5.00, 5.01, 5.03, 5.12, 5.22
h-LNMO-4	3.02, 3.00, 14.65	0.76	4.69, 4.71 (×2), 4.81, 5.46, 5.49, 5.50, 5.59
m-LNMO	5.03, 8.69, 9.79	2.44	5.14, 5.15, 5.16 (×5)

Table S8. Magnetic moment of Ru (μ_{Ru}), band gap (E_g), and defect formation energies ($E_f(Ru_{Mn})$) for Ru-doping of h-LNMO. Ru_{Mn} signifies if the Ru-dopant is located on an Mn-site.

System	μ_{Ru} (μ_B)	E_g (eV)	$E_f(Ru_{Mn})$ (eV)
Ru_{Mn}	1.49	0.57	4.99
Ru_{Mn}	1.57	0.48	5.12
Ru_{Mn}	1.57	0.71	4.84
Ru_{Mn}	1.47	0.60	5.03
Ru_{Mn}	1.57	0.53	5.22
Ru_{Mn}	1.50	0.70	4.84
Ru_{Mn}	1.47	0.64	5.01
Ru_{Mn}	1.48	0.59	5.00
Ru_{Mn}	1.26	0.00	5.50
Ru_{Mn}	1.57	0.82	4.81
Ru_{Mn}	1.27	0.13	5.46
Ru_{Mn}	1.54	0.54	4.71
Ru_{Mn}	1.33	0.00	5.59
Ru_{Mn}	1.57	0.51	4.69
Ru_{Mn}	1.56	0.73	4.71
Ru_{Mn}	1.31	0.00	5.49
Ru_{Mn}	1.23	0.20	5.53
Ru_{Mn}	1.56	0.62	4.61
Ru_{Mn}	1.58	0.64	4.71
Ru_{Mn}	1.23	0.00	4.61
Ru_{Mn}	1.23	0.18	5.50
Ru_{Mn}	1.57	0.71	4.79
Ru_{Mn}	1.53	0.63	4.83
Ru_{Mn}	1.26	0.00	5.61
Ru_{Mn}	1.46	0.35	5.07
Ru_{Mn}	1.50	0.41	5.11
Ru_{Mn}	1.54	0.36	5.08
Ru_{Mn}	1.55	0.80	4.69
Ru_{Mn}	1.48	0.33	5.09
Ru_{Mn}	1.55	0.80	4.73
Ru_{Mn}	1.56	0.34	5.01
Ru_{Mn}	1.52	0.35	5.03

Table S9. Magnetic moment of Ru (μ_{Ru}), band gap (E_g), and defect formation energies ($E_f(Ru_{Mn})$) for Ru-doping of m-LNMO.

System	μ_{Ru} (μ_B)	E_g (eV)	$E_f(Ru_{TM})$ (eV)
Ru_{Mn}	1.56	0.54	5.16
Ru_{Mn}	1.51	0.66	5.16
Ru_{Mn}	1.57	0.56	5.14
Ru_{Mn}	1.50	0.67	5.15
Ru_{Mn}	1.56	0.54	5.16
Ru_{Mn}	1.56	0.52	5.16
Ru_{Mn}	1.56	0.59	5.15
Ru_{Mn}	1.56	0.54	5.16

Table S10. Average, minimum, and maximum oxygen vacancy defect formation energies in the undoped and Ru-doped LNMO phases.

Phase	System	Average (eV)	Min (eV)	Max (eV)
Hexagonal	Undoped	2.52	2.10	3.43
	Ru_{Mn}	2.78	1.88	4.35
Monoclinic	Undoped	2.24	2.14	2.44
	Ru_{Mn}	2.42	2.01	3.28

SUPPORTING INFORMATION

References

[1] K.-D. Liss, B. Hunter, M. Hagen, T. Noakes, S. Kennedy, *J. Phys. Condens. Matter* **2006**, *385-386*, 1010-1012.
[2] B. H. Toby, R. B. Von Dreele, *J. Appl .Crystallogr.* **2013**, *46*, 544-549.
[3] J. Neuefeind, M. Feygenson, J. Carruth, R. Hoffmann, K. K. Chipley, *Nucl. Instrum. Methods Phys. Res., Sect. B* **2012**, *287*, 68-75.
[4] C. Farrow, P. Juhas, J. Liu, D. Bryndin, E. Božin, J. Bloch, T. Proffen, S. Billinge, *J. Phys. Condens. Matter* **2007**, *19*, 335219.
[5] B. C. C. Cowie, A. Tadich, L. Thomsen, *AIP Conf. Proc.* **2010**, *1234*, 307-310.
[6] B. Ravel, M. Newville, *J. Synchrotron Radiat.* **2005**, *12*, 537-541.
[7] G. Liang, J. Hao, A. M. D'Angelo, V. K. Peterson, Z. Guo, W. K. Pang, *Batter. Supercaps* **2021**, *4*, 380-384.
[8] K. S. Wallwork, B. J. Kennedy, D. Wang, *AIP Conf. Proc.* **2007**, *879*, 879-882.
[9] a) J. J. Mortensen, L. B. Hansen, K. W. Jacobsen, *Phys. Rev. B* **2005**, *71*, 035109; b) J. Enkovaara, C. Rostgaard, J. J. Mortensen, J. Chen, M. Dułak, L. Ferrighi, J. Gavnholt, C. Glinsvad, V. Haikola, H. Hansen, *J. Phys. Condens. matter* **2010**, *22*, 253202.
[10] P. E. Blöchl, *Phys. Rev. B* **1994**, *50*, 17953.
[11] A. H. Larsen, J. J. Mortensen, J. Blomqvist, I. E. Castelli, R. Christensen, M. Dułak, J. Friis, M. N. Groves, B. Hammer, C. Hargus, *J. Phys. Condens. Matter* **2017**, *29*, 273002.
[12] J. P. Perdew, K. Burke, M. Ernzerhof, *Phys. Rev. Lett* **1996**, *77*, 3865.
[13] H. J. Monkhorst, J. D. Pack, *Phys. Rev. B* **1976**, *13*, 5188.
[14] S. L. Dudarev, G. A. Botton, S. Y. Savrasov, C. Humphreys, A. P. Sutton, *Phys. Rev. B* **1998**, *57*, 1505.
[15] a) S. Nachimuthu, H.-W. Huang, K.-Y. Lin, C. Yu, J.-C. Jiang, *Appl. Surf. Sci.* **2021**, *563*, 150334; b) Y. Wang, F. Li, H. Zheng, X. Han, Y. Yan, *Phys. Chem. Chem. Phys.* **2018**, *20*, 28162-28168; c) H.-S. Kim, A. Catuneanu, H.-Y. Kee, *Phys. Rev. B* **2015**, *91*, 241110.
[16] J. Zhang, Q. Wang, S. Li, Z. Jiang, S. Tan, X. Wang, K. Zhang, Q. Yuan, S. J. Lee, C. J. Titus, K. D. Irwin, D. Nordlund, J. S. Lee, P. Pianetta, X. Yu, X. Xiao, X. Q. Yang, E. Hu, Y. Liu, *Nat. Commun.* **2020**, *11*, 6342.
[17] J. R. Croy, H. Iddir, K. Gallagher, C. S. Johnson, R. Benedek, M. Balasubramanian, *Phys. Chem. Chem. Phys.* **2015**, *17*, 24382-24391.
[18] a) N. Li, S. Hwang, M. Sun, Y. Fu, V. S. Battaglia, D. Su, W. Tong, *Adv. Energy Mater.* **2019**, *9*, 1902258; b) J. S. Kim, B. H. Kim, D. C. Kim, H. J. Lee, M. G. Kim, A. Maignan, B. Raveau, Y. W. Park, *J. Superconductivity* **2004**, *17*, 183-186.
[19] K. Okhotnikov, T. Charpentier, S. Cadars, *J. Cheminform.* **2016**, *8*, 1-15.
[20] S. Zhang, J. E. Northrup, *Phys. Rev. Lett.* **1991**, *67*, 2339.
[21] F. Kröger, H. Vink, in *Solid State Phys., Vol. 3*, Elsevier, **1956**, pp. 307-435.
[22] a) A. Chakraborty, S. Kunnikuruvan, S. Kumar, B. Markovsky, D. Aurbach, M. Dixit, D. T. Major, *Chem. Mater.* **2020**, *32*, 915-952; b) E. Olsson, J. Cottom, X. Aparicio-Angles, N. H. de Leeuw, *Phys. Chem. Chem. Phys.* **2019**, *21*, 9407-9418; c) G. Liang, E. Olsson, J. Zou, Z. Wu, J. Li, C. Z. Lu, A. M. D'Angelo, B. Johannessen, L. Thomsen, B. Cowie, V. K. Peterson, Q. Cai, W. K. Pang, Z. Guo, *Angew. Chem. Int. Ed.* **2022**, e202201969.
[23] K. Momma, F. Izumi, *J. Appl. Crystallogr.* **2011**, *44*, 1272-1276.
[24] L. Bao, L. Wei, N. Fu, J. Dong, L. Chen, Y. Su, N. Li, Y. Lu, Y. Li, S. Chen, *J. Energy Chem.* **2022**, *66*, 123-132.
[25] E. Zhao, X. Liu, H. Zhao, X. Xiao, Z. Hu, *Chem. Commun.* **2015**, *51*, 9093-9096.
[26] C. Zhang, B. Wei, W. Jiang, M. Wang, W. Hu, C. Liang, T. Wang, L. Chen, R. Zhang, P. Wang, W. Wei, *ACS Appl. Mater. Interfaces* **2021**, *13*, 45619-45629.
[27] T. Lin, T. U. Schulli, Y. Hu, X. Zhu, Q. Gu, B. Luo, B. Cowie, L. Wang, *Adv. Funct. Mater.* **2020**, *30*, 1909192.
[28] H. Liu, W. Xiang, C. Bai, L. Qiu, C. Wu, G. Wang, Y. Liu, Y. Song, Z.-G. Wu, X. Guo, *Ind. Eng. Chem. Res.* **2020**, *59*, 19312-19321.
[29] A. Abdel-Ghany, A. M. Hashem, A. Mauger, C. M. Julien, *Energies* **2020**, *13*, 3487.
[30] X. Ding, D. Luo, J. Cui, H. Xie, Q. Ren, Z. Lin, *Angew. Chem. Int. Ed.* **2020**, *59*, 7778-7782.
[31] M. Chen, X. Jin, Z. Chen, Y. Zhong, Y. Liao, Y. Qiu, G. Cao, W. Li, *J. Mater. Chem. A* **2019**, *7*, 13120-13129.
[32] F. Wu, G. T. Kim, M. Kuenzel, H. Zhang, J. Asenbauer, D. Geiger, U. Kaiser, S. Passerini, *Adv. Energy Mater.* **2019**, *9*, 1902445.
[33] C. Han, J. Wu, S. Li, T. Li, J. Li, H. Liu, *Solid State Ion.* **2021**, *364*, 115629.
[34] J. Zhang, Q. Zhang, D. Wong, N. Zhang, G. Ren, L. Gu, C. Schulz, L. He, Y. Yu, X. Liu, *Nat. Commun.* **2021**, *12*, 3071.
[35] P. Bindu, S. Thomas, *Journal of Theoretical and Applied Physics* **2014**, *8*, 123-134.